Chaos, Solitons and Fractals 122 (2019) 6–16

Contents lists available at ScienceDirect

Chaos, Solitons and Fractals

Nonlinear Science, and Nonequilibrium and Complex Phenomena

journal homepage: www.elsevier.com/locate/chaos

Nonlinear dynamics and chaos in micro/nanoelectromechanical beam resonators actuated by two-sided electrodes

André Gusso[a,b,*], Ricardo L. Viana[b], Amanda C. Mathias[c], Iberê L. Caldas[c]

[a] Departamento de Ciências Exatas-EEIMVR, Universidade Federal Fluminense, Volta Redonda, RJ 27255-125, Brazil
[b] Departamento de Física, Universidade Federal do Paraná, Curitiba, PR 81531-980, Brazil
[c] Departmento de Física Aplicada, Instituto de Física da Universidade de São Paulo, São Paulo, SP 05508-090, Brazil

ARTICLE INFO

Article history:
Received 30 November 2018
Revised 28 February 2019
Accepted 2 March 2019
Available online 15 March 2019

Keywords:
Nonlinear dynamics
Chaos
Basin entropy
Microelectromechanical systems
Nanoelectromechanical systems

ABSTRACT

We investigate theoretically the nonlinear dynamics and the emergence of chaos in suspended beam micro/nanoelectromechanical (MEMS/NEMS) resonators actuated by two-sided electrodes. Through the analysis of phase diagrams we have found that the system presents a rich and complex nonlinear behavior. Multistability is observed in a significant region of the relevant parameter space, involving periodic and chaotic attractors. Complex and varied routes to chaos were also found. Basins of attraction with strongly intermingled attractors provide further evidence of multistability. The basins are analyzed in greater detail. Their fractal dimensions and uncertainty exponent are calculated using the well known box counting and uncertainty methods. The results for the uncertainty exponent are compared with those obtained with yet another approach, based on the recently proposed basin entropy method. The comparison provides a test for the new approach, which we conclude that is a reliable alternative method of calculation. Very low uncertainty exponents have been obtained, indicating that some basins have extremely intermingled attractors, what may have significant influence in the experimental investigation and practical applications of the resonators. We also conclude that the observation of chaos in this system is favored by lower frequencies of excitation and comparatively small quality factors (larger dissipation).

1. Introduction

MEMS/NEMS resonators based on suspended beams are one of the most investigated micro/nanodevices, both theoretically and experimentally [1,2]. They have many potential applications, for instance, as high quality factor filters for electronic signals, ultrastable reference clocks and a variety of physical and chemical sensors, that rely upon their operation in a linear regime [1,2]. For a long time the ease with which these small systems can enter the nonlinear regime, due to the electrostatic force and midplane stretching, was seen as a significant problem. However, more recently, some strategies to take advantage of the nonlinear behavior have been proposed to improve signal amplification [3] and frequency stability [4], among other applications [5]. The existence of chaos in suspended beam resonators was predicted theoretically in several works [6–10] and verified experimentally for two coupled nanomechanical beam resonators [11]. So far, the potential use of the chaotic regime of these systems was only briefly investigated theoretically [8]. However, as already proposed for other configurations of MEMS/NEMS resonators [12], suspended beam resonators have the potential to be used as sources of chaotic signals for applications in chaos based secure communications, cryptography and random number generation. Because of their smallness, high frequency of vibration and low power consumption, suspended beam MEMS/NEMS resonators are ideal candidates as a physical source of continuous chaotic signal or entropy in mobile devices.

Motivated by these reasons, some aspects of the chaotic dynamics of a doubly clamped (bridge) suspended beam MEMS/NEMS resonator actuated by two lateral electrodes were investigated by Dantas and Gusso [10]. This particular system was considered because its is frequently found in the investigation of potential applications of suspended beam MEMS/NEMS resonators [2] and because chaos can be more easily obtained with a two electrodes configuration [8]. We note that other similar systems, particularly the case of a plate suspended between two electrodes, have also had its nonlinear and chaotic dynamics investigated [13,14]. However, there is still a great deal to be understood about the

---

[*] Corresponding author: Departamento de Ciências Exatas-EEIMVR, Universidade Federal Fluminense, Volta Redonda, RJ 27255-125, Brazil.
E-mail address: andregusso@id.uff.br (A. Gusso).

https://doi.org/10.1016/j.chaos.2019.03.004

nonlinear and chaotic dynamics of such systems. A thorough theoretical understanding is necessary for the experimental investigation and practical application of such devices. For this reason, in this work we extended the previous analysis which focused mostly on the chaotic regime of a doubly clamped suspended beam MEMS/NEMS resonator actuated by two-sided electrodes [10]. We investigate the regions in the relevant parameter space where periodic behavior, chaos and pull-in (the snap down and stiction of the beam onto the electrodes) can occur, and present phase diagrams for the system. We reveal the complex structure of attractors around the regions with chaos which had not been investigated previously. We find significant regions with signs of multistability, a relevant fact, with potentially significant practical implications, which have not been reported to this system in the literature. Because the initial conditions of the system can be strongly affected by noise and, in the case of a system with double-well potential, by the instabilities inherent to the system, we have investigated the basins of attraction along several regions indicated in the phase diagrams. Such analysis was completely missing in [10] and in the known literature. Analyzing the basins of attraction we have been able to confirm the multistability indicated in phase diagrams. We obtain interesting results regarding their structure, fractal dimension and uncertainty exponent.

The work is organized as follows. In Section 2 we present the physical and mathematical model of the MEMS/NEMS resonator. Phase diagrams are presented in Section 3, and basins of attraction are presented in Section 4 and analyzed in Section 5. We discuss the results obtained and summarize our conclusions in Section 6.

2. Physical and mathematical model

The device we are going to investigate is comprised of a slender beam with length l and with a rectangular cross section of width b and thickness h. The beam is clamped at both ends and there are electrodes parallel to its width placed a distance d at both sides of the beam. This arrangement is depicted schematically in Fig. 1. As done in [10,15] we are going to consider a device with realistic dimensions and physical properties.

The beam is considered to have homogeneous and isotropic elastic properties, and due to its slenderness the Euler-Bernoulli beam theory can be used to model the beam. Because in the strong nonlinear regime that we investigate here the beam can be subject to large transversal displacements, compared to its thickness, we have to include the effect of the midplane stretching [16]. It is responsible for a nonlinear hardening effect of the elastic restoring force. Because we are going to consider a beam with $d \ll h$, the beam bending is going to small and the electrostatic force can be modeled assuming that the beam is piecewise plane. Also, we consider that the beam will be sufficiently wide that the parallel plate approximation for the electrostatic force can be used and the fringing effect ignored. Finally, assuming as usually done that dissipation occurs due to a viscous damping, the partial differential equation modeling the system results to be [10]

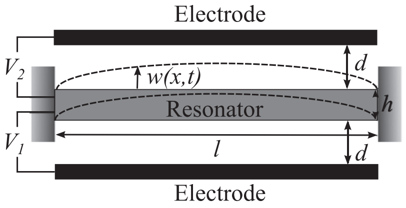

Fig. 1. Schematic diagram of the doubly clamped suspended beam resonator (gray) with two lateral electrodes (black).

$$EIw'''' + \rho A\ddot{w} + c\dot{w} - \left(\frac{EA}{2l}\int_0^l w'^2 dx\right)w'' + \frac{\epsilon_0 b}{2}\left[\frac{V_1(t)^2}{(d+w)^2} - \frac{V_2(t)^2}{(d-w)^2}\right] = 0. \tag{1}$$

In this equation $w(x, t)$ corresponds to the vertical displacement along the beam, subject to the boundary conditions $w(0,t) = w(l,t) = w'(0,t) = w'(l,t) = 0$. It is comprised between $x = 0$ and $x = l$ and is placed a distance d from both electrodes. The overdots and primes represent derivatives with respect to time t, and space x, respectively. E denotes the Young modulus and ρ the density of the beam material. $I = bh^3/12$ corresponds to the geometric moment of inertia, $A = bh$ to its cross-sectional area, and c to the linear damping coefficient. The beam is subject to the electrostatic potentials V_1 and V_2, and $\epsilon_0 = 8.85 \times 10^{-12}$ F/m corresponds to the vacuum permittivity.

As explained in details in [10] the first two terms in Eq. (1) correspond to the elastic and inertia terms of the Euler-Bernoulli beam theory, and the third term to the viscous damping. The term proportional to w'' corresponds to the nonlinear restoring force due to the midplane stretching. The last term gives the contribution of the electrostatic force, which is obtained assuming that the beam is piecewise plane. We note that we are ignoring the fringing effect because, as already argued in [10], the correction for the particular system that we consider is expected to be small compared to the main effects already taken into account in our model.

We do not solve Eq. (1) directly, instead, we resort to the Galerkin method to reduce this equation to a single nonlinear ordinary differential equation (NLODE). Using a single mode approximation we take $w(x,t) = u(t)\phi_1(x)$, where $\phi_1(x)$ denotes the base function which corresponds to the first modeshape of a doubly clamped beam described mathematically by the Euler-Bernoulli beam equation [16]. This approximation is justified, among other reasons, because we are interested in the description of the dynamics of the beam oscillating in its first mode of vibration. This mode is preferred in practical applications because it results in the best read-out of the oscillations, providing a better information about the position of the beam during vibration. The use of the modeshape of an Euler-Bernoulli beam to approximate the nonlinear beam shape is adequate for frequencies below and around the first resonance frequency. Furthermore, the use of a single mode approximation to describe the temporal dynamics of the chaotic regime of beams and cables is well justified in the literature, both theoretically and experimentally (see the discussion in [10] and references therein).

Following the Galerkin method, we can obtain a NLODE for the coordinate $u(t)$ which, upon suitable rescaling, results in the equation

$$\ddot{s} + \beta\dot{s} + s + \alpha s^3 + F^e(s,\tau) = 0. \tag{2}$$

In this NLODE $s = s(\tau)$ is the nondimensional displacement of the beam center. More specifically, $s(\tau) = u(\tau)w_{\max}/d$, where $w_{\max} = w(x = 0.5l, \tau)$ corresponds to the maximum beam displacement that occurs at $x = 0.5l$. Time t is replaced by the nondimensional time $\tau = t/\omega_1$, where ω_1 denotes the natural frequency of the first mode. The strength of the cubic nonlinearity is $\alpha = 0.719(d/h)^2$, and the damping factor $\beta = c/\rho bh\omega_1$ can be shown to be related to the quality factor Q simply by $\beta = Q^{-1}$.

The last term in Eq. (2) corresponds to the effective electrostatic force, and is given by

$$
\begin{aligned}
F^e(s,\tau) &= 1.218\frac{\epsilon_0 bl}{2k_{eff}d^3}\Big[V_1^2(\tau)\int_0^1 \frac{\phi_1(x')}{(1+\phi_1(x')s/d)^2}dx' \\
&\quad -V_2^2(\tau)\int_0^1 \frac{\phi_1(x')}{(1-\phi_1(x')s/d)^2}dx'\Big] \\
&= B\big[V_1^2(\tau)I^e(s) - V_2^2(\tau)I^e(-s)\big], \qquad (3)
\end{aligned}
$$

where $B = 0.609\epsilon_0 bl/(k_{eff}d^3)$, and $k_{eff} = 384EI/l^3$ denotes the effective elastic constant of the beam and the new variable x' is the normalized length position $x' = x/l$.

Eq. (2) is, therefore, an integro-differential equation, whose direct numerical solution is computationally quite demanding because it involves to solve two integrals numerically. In order to solve this NLODE in a efficient manner, we follow the procedure adopted in [7,10,15] and replace $F^e(s,\tau)$ by a function of the form

$$
I_a^e(s) = \frac{a_0 + a_1 s}{(1+\sum_{i=1}^3 b_i s^i)}, \qquad (4)
$$

which we can recognize as a Padé approximant of order 1/3. The coefficients a_i and b_i are obtained using the least squares fit so that $I_a^e(s)$ is close enough to the value of $I^e(s)$ obtained by numerical integration within a suitable interval in the variable s. In the present analysis we have to warrant a sufficiently high accuracy for $I_a^e(s)$ in the range $-0.8 \le s \le 0.8$, which encompasses the initial conditions (ICs) used in the basins of attraction we have investigated. We have also to take into account that the solutions cannot be outside the interval $|s| < 1$, because the electrodes are located at $s = \pm 1$, and if s comes sufficiently close to the electrodes the system will fatally stop to oscillate due to the dynamical pull-in (the beam is attracted and gets attached to one of the electrodes due to the electrostatic force caused by the applied DC bias voltage, V_{DC}). In practice, we stop the numerical calculations when $|s|$ exceeds a certain value, which we take to be $|s| = 0.9$ (the results involving the pull-in do not change if we take a larger threshold). Using the Padé approximant of order 1/3 it is possible to obtain a maximum error of about 0.1% in the approximation to the function $I^e(s)$ within the interval $|s| < 0.8$, the average error being much smaller than that. The approximation is still quite reliable outside this interval up to the point where the system is considered to have suffered pull-in.

The applied voltages $V_1(\tau)$ and $V_2(\tau)$ are responsible for the resulting effective static potential of the system. Constant (DC) voltages applied to the electrodes have the important effect of altering the effective spring constant. Due to this effect, the resulting effective static potential has a single stable minimum, for small applied DC voltages, but develops a potential with two minima for sufficiently high voltages [8,10]. This is illustrated by the potentials in Fig. 2. The voltages are also used to drive the system. In this work we consider the case in which the driving alternating (AC) voltage is applied to only one of the electrodes. This is what is generally done in practical systems because the resulting oscillations are read out through the second electrode. For definiteness we are going to consider that the applied voltages are $V_1(\tau) = V_{DC} + V_{AC}\cos(\zeta\tau)$ and $V_2(\tau) = V_{DC}$.

With the applied voltages the resulting dynamical system has interesting features. They can be more easily observed if we consider the limit of small amplitude of oscillation and expand Eq. (2) in a Taylor series in s up to third order. The result is

$$
\ddot{s} + \beta\dot{s} + k_1(\tau)s + k_2(\tau)s^2 + k_3(\tau)s^3 + F(\tau) = 0, \qquad (5)
$$

where

$$
\begin{aligned}
k_1(\tau) &= 1 + \gamma\big[(a_1 - a_0 b_1)(V_{AC}(\tau) + V_{DC})^2 - a_1(b_1 + a_1)V_{DC}^2\big], \\
k_2(\tau) &= \gamma\Big\{-\big[a_0\big(b_1^2 - b_2\big) - a_1 b_1\big](V_{AC}(\tau) + V_{DC})^2 \\
&\quad + a_1(b_1^2 - b_2 - b_1)V_{DC}^2\Big\},
\end{aligned}
$$

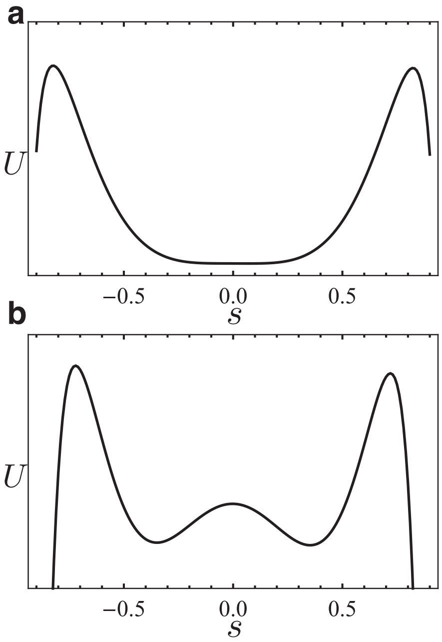

Fig. 2. Representative examples of the effective potential energy U (arbitrary units) as a function of the beam displacement s for the case of (a) one-well and (b) double-well potentials.

$$
\begin{aligned}
k_3(\tau) &= \alpha + \gamma\Big\{-\big[a_0\big(b_1^3 - 2b_2 b_1 + b_3\big) - a_1\big(b_1^2 - b_2\big)\big](V_{AC}(\tau) \\
&\quad + V_{DC})^2 - a_1 b_1^3 V_{DC}^2 + a_1(b_1^2 + 2b_2 b_1 - b_2 - b_3)V_{DC}^2\Big\}, \qquad (6)
\end{aligned}
$$

and

$$
F(\tau) = \gamma\big[a_1 V_{DC}^2 - a_0(V_{AC}(\tau) + V_{DC})^2\big]. \qquad (7)
$$

The parameter γ is defined as

$$
\gamma = \frac{1.218\epsilon_0\, hl}{2d^3 k_{eff}}. \qquad (8)
$$

What we have obtained in Eq. (5) is a Helmholtz-Duffing like equation, but with time dependent coefficients. The time dependence is due to the applied AC voltage, $V_{AC}(\tau) = V_{AC}\cos(\zeta\tau)$. Therefore, the system is parametrically excited through all of its linear and nonlinear coefficients of the restoring force. However, the system is also excited by an external force term, $F(\tau)$. This mixing of external and parametric excitation may explain the rich and complex nonlinear dynamics that we present in the next section. It is important to note that, while the idea of the system having an effective static potential due to the applied voltages is useful to understand some aspects of its dynamics [10], the system does not have a definite potential energy due to the parametric excitation.

3. Phase diagrams

In this and the next sections we present results for the nonlinear dynamics of a nanoresonator, characterized by having two of its dimensions in the submicrometer range. We consider a realistic device with dimensions $l = 5$µm, $b = 0.8$µm and $h = 0.05$µm. The gap is chosen based upon a criteria that facilitates the appearance of a double-well potential [8,10], which favors a chaotic dynamics, and is taken to be $d = 0.15$µm. The device is considered to be made of polysilicon, whose Young modulus is $E = 170$ GPa and the density $\rho = 2.3 \times 10^3$ kg m^{-3} [16]. With these dimensions and materials, the predicted natural frequency of the first mode is $f = 17.7$ MHz, in the absence of any applied voltage.

We have to note that for gaps in the submicrometer range it has been customary to take into account the effects of the Casimir force in the modelling of the system [7,16]. However, it was already shown that this quantum mechanical force is relevant only for similar systems with gaps of the order of a few tens of nanometers [7], therefore, much smaller than the one considered in our case. We also note that for such a small device, surface elasticity effects could contribute [9]. However, the exact effect depends crucially on the elastic properties of the surface and the model of size effects. Furthermore, the contributions of surface roughness and the presence of oxides have been ignored in the models presented in the literature. Because significant surface roughness and oxides, or other surfaces contaminants, are almost always present, any surface modelling would result imprecise or unrealistic. For these reasons, and because the surface effects are expected to be particularly small for silicon beams [17], we also ignore its possible contribution.

The rich and complex nonlinear dynamics of this system is evidenced in the phase diagrams presented in Fig. 3. These diagrams show in the $V_{AC} - V_{DC}$ plane the periodic (see color code in the figure caption) and chaotic attractors (black regions), and the pull-in states (purple and red). The results are presented for three representative frequencies $\zeta = 0.2, 0.4,$ and 0.6 and two damping coefficients $\beta = 0.01$ and 0.001. The larger damping coefficient is representative of devices operating in air, while the lower dissipation is more easily found in devices operating in vacuum.

The region chosen in the $V_{AC} - V_{DC}$ plane is the one containing the more interesting features of the dynamics. It is dominated by periodic dynamics, mostly with period-1 attractors. We can see that there are sub-regions with smooth boundaries between the different attractors. However, there are regions where the boundaries are very complex and those where the attractors are strongly intermingled. This is clearly exemplified by the region close to the black cross in Fig. 3 (c) containing a region with mixed period-1 and period-3 attractors. This mixing of the attractors is stronger for lower dissipation and higher frequencies, as evidenced in Figs. 3 (d),(e) and (f). We note that the mixing for the lower dissipation has remained stronger in spite of the fact that the results presented in Figs. 3 (d),(e) and (f) have been obtained after a long transient of 7000 times the period of the driving frequency, while the results for higher dissipation have been obtained for a transient of 3500 periods. The observed mixing of the attractors is reflected in the basins of attraction, as we are going to present in more detail later. These results indicate the existence of multistability in these regions. The multistability may have significant consequences such as noise-induced jumps between different attractors, what prevents the predictability of the final state along these regions in the presence of noise [18].

For this system there are comparatively large regions with chaos for low frequencies, as illustrated for $\zeta = 0.2$ in Fig. 3(a), independently of β. However, these regions tend to decrease and disappear as the frequency increases. For instance, only a small iso-

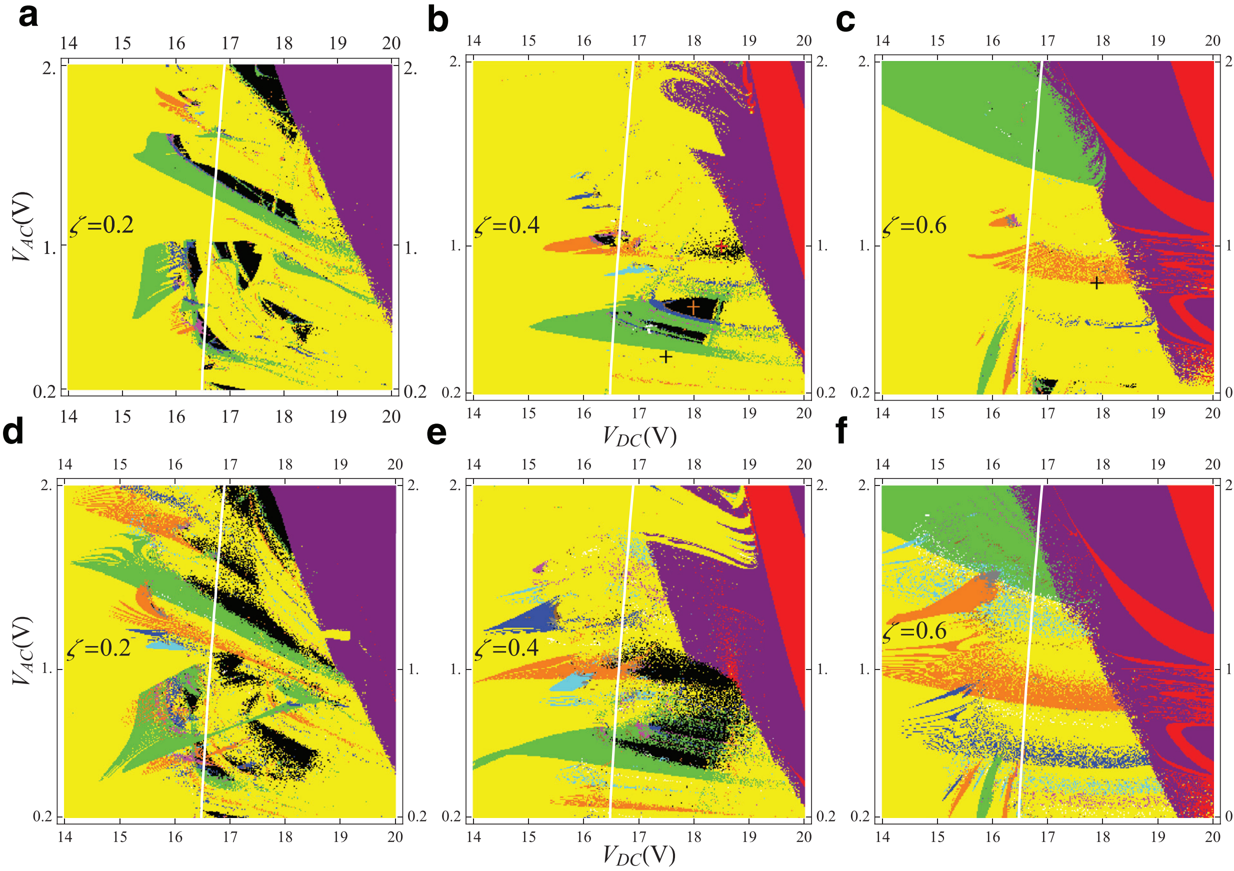

Fig. 3. Phase diagrams in the $V_{AC} - V_{DC}$ plane for different frequencies ζ, showing the periodic, chaotic and pull-in attractors. The phase diagrams (a), (b), and (c) have been calculated for $\beta = 0.01$ while (d), (e), and (f) have been calculated for $\beta = 0.001$. The white line is the separatrix between the regions with one-well potential to the left and double-well effective potential to the right. The color code is the following. For the periodic attractors: yellow (period T), green (2T), orange (3T), blue (4T), cyan (5T), magenta (6T), white (7T), brown (8T). Periods above $9T$ are colored gray. The pull-in to the electrode located at $s = -1 (s = 1)$ is colored red(purple), and chaos is presented in black. The crosses denote points whose basins of attraction are presented in Sections 4 and 5 (see text for more details). (For interpretation of the references to colour in this figure legend, the reader is referred to the web version of this article.)

lated island is left for $\zeta = 0.6$ for the larger dissipation $\beta = 0.01$, and no chaos is observed for $\beta = 0.001$.

In the phase diagrams we have drawn the line separating the regions in which the effective potential has one and two local minima around the central region. We can see that most of the regions with chaos are located in the double-well region, as it was expected [8] due to cross-well chaos. However, there are also regions with chaos in the one-well region, particularly for low frequencies.

It is also possible to see from the phase diagrams that for $\beta = 0.01$ and for the lower frequencies, the prevailing route to chaos is period doubling, but other routes are also present. For lower dissipation, the multistability prevents the observation of sharp boundaries between attractors and the routes to chaos are far less evident.

The role of dissipation is not restricted to increase the regions with possible multistability and blur the boundaries between the different attractors as it decreases. It also reduces the required voltages for the system to suffer pull-in, as it is evidenced by the displacement of the boundaries between the periodic and chaotic attractors and the region with pull-in. This effect results in the larger areas with pull-in obtained for $\beta = 0.001$ as compared with $\beta = 0.01$. From Figs. 3 (d), (e), and (f) we can see that a smaller dissipation also results in an increase of the regions where higher periods are observed for all frequencies.

From the analysis of the phase diagrams we can conclude that experiments aiming at finding chaos in this NEMS resonator and for its practical applications as a source of chaotic signal, the system should be driven preferentially at frequencies $\zeta \lesssim 0.4$, where the chances of finding a region with chaos is larger. Also, a higher dissipation, around $\beta = 0.01$, favors the existence of regions with chaos which do not contain significant signs of multistability, that could inadvertently turn chaos into an undesirable periodic behavior.

4. Basins of attraction

As illustrated in Fig. 2, the nanoresonator can be subject to either a one-well or double-well effective potential, depending on the applied V_{DC} and V_{AC} voltages. Let us consider that the DC voltage is applied before the AC voltage. That is a likely scenario in an actual system, since the AC voltage would be generated by an external oscillator that should have its voltage amplitude and frequency stabilized before it could drive the MEMS/NEMS resonator. In the absence of an applied AC voltage, the minimum of the one-well potential is located very close to $s = 0$, coinciding with the rest position in the absence of any external forces. In this case, the IC at $\tau = 0$, the time the AC voltage starts driving the system is close to $s(0) = v(0) = 0$. We say that it is close to these values because, for instance, fabrication tolerances can result in small gap asymmetries and, consequently, asymmetries in the initial potential energy that affect the location of the potential minimum. More importantly, thermal noise and external vibrations cause s and v to fluctuate around the minimum of the static potential before the V_{AC} is applied [19]. These fluctuations can be rather large as V_{DC} approaches the voltage required to have two minima in the potential. In this case the one-well potential develops a flat bottom, as illustrated by the potential in Fig. 2(a) and, consequently, the effective linear elastic constant, given by the curvature of the potential bottom, can be rather small allowing large fluctuations of s and v. The scenario for the ICs can be even more complex for a double-well potential. In this case, a resonator initially at the rest position at $s = 0$, now an unstable local maximum, under the influence of thermal noise and external vibrations, would tend to slide to one of the two potential minima. Therefore, the most likely ICs for the system are those with s close to either one of the two minima, the specific value also fluctuating due to noise. For the voltages we consider in our analysis, in the absence of an applied V_{AC}, one of two minima is usually between $s \sim 0.2$ and 0.5 and the other between $s \sim -0.2$ and -0.5. Because the ICs in an actual device can assume different values in a significant range of s and v, the investigation of the basins of attraction of the nanoresonator are justified not only by pure theoretical reasons, but also because they can have implications to the real systems.

To investigate the basins of attraction we started by generating hundreds of basins in the parameter space region defined by $16\,\text{V} \leq V_{DC} \leq 19$ V, $0.2\,\text{V} \leq V_{AC} \leq 1.2$ V, and $0.2 \leq \zeta \leq 0.6$. The ICs were in the range $-0.8 \leq s, v \leq 0.8$, which encompasses a region with practical and theoretical relevance. For larger absolute values of these parameters, most of the final states correspond to pull-in.

In the region of the parameter space (V_{AC}, V_{DC}, ζ) that we have investigated, most of the basins present only three attractors, namely, pull-in to the electrode at $s = -1$, pull-in to the electrode at $s = 1$, and a periodic or chaotic attractor. These basins present a simple topology with the periodic and chaotic attractors encompassing a continuous region having smooth boundaries defined by the two pull-in attractors. Two such basins are exemplified in Figs. 4(a) and (b). They have been obtained for the parameters corresponding to the points indicated by the black and orange crosses in Fig. 3(b), respectively. Also, a very small fraction is found that mixes more than three attractors in a comparatively simple topology, like the one illustrated by Fig. 4(c). Basins such as these in Fig. 4 are found in the regions in the phase diagrams that are not close to or within the regions where basins are intermingled.

We have also found a significant fraction of more complex basins, with intermingled periodic and/or chaotic attractors. Quite generally, such basins are found close to or within the regions

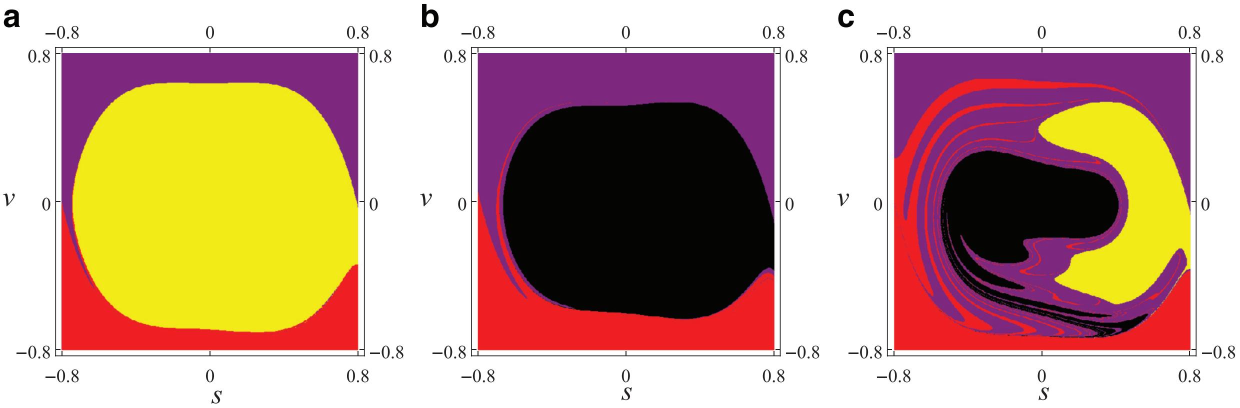

Fig. 4. Basins of attraction for varying initial conditions s and v. (a) $V_{AC} = 0.4$ V, $V_{DC} = 17.5$ V and $\zeta = 0.4$, (b) $V_{AC} = 0.67$ V, $V_{DC} = 18$ V and $\zeta = 0.4$, and (c) $V_{AC} = 0.651$ V, $V_{DC} = 17.4$ V and $\zeta = 0.88$. In all cases $\beta = 0.01$. The color code is the same as that presented in the caption of Fig. 3.

in the phase diagram where the attractors are also intermingled. One such basin is presented in Fig. 5(a). It was obtained for parameters in a region with mixed attractors, indicated by the red cross in Fig. 3(b). In this basin we have period-1 and period-3 attractors which are mixed in a complex manner within the region surrounded by the pull-in attractors. The two periodic attractors seems to form a fractal basin. The fractality of the attractor is evidenced in Figs. 5(b) and (c) where we present magnified views of the basin. While other basins have been found that have a structure suggestive of an usual fractal basin, most of the basins containing mixed periodic or chaotic attractors had a topology that is exemplified by the basins presented in Figs. 6 and 7. What we see are strongly intermingled basins. Their fractality was checked through the numerical calculation of the stable and unstable manifolds of saddle fixed points. The two manifolds have been found to have homoclinic intersection points that form a chaotic invariant set which imply in a fractal basin boundary defined by the stable manifold [20,21]. However, while for the basin in Fig. 6 we can see some structures in the form of small islands, lines and curves, that rapidly vanish due to the finite resolution of the grid used for the calculations, the basin in Fig. 7 has shown no such structures. That is the reason why we have shown a single larger magnification of a smaller region in Fig. 7(b).

The existence of such basins, with strongly mixed attractors, confirms the existence of multistability in the system. Multistability is an interesting phenomenon appearing in nonlinear systems that can be explored for certain applications [3], but can also prevent the correct operation of the system. For example, that could be the case if the NEMS resonator was operated as a source of chaotic signals close to or at a region with multistability. Due to noise, the system could constantly shift from a chaotic to a periodic state [18]. This could happen due to fabrication tolerances, that may lead the system to operate in a region of the parameter space that was not initially intended.

So far, we have discussed only qualitative aspects of the fractal basins found in the regions of the phase space with mixed attractors. However, the observed strong mixing between attractors within the region surrounded by the pull-in attractors deserves to be quantified. We can get information regarding how intermingled are the attractors and what is the uncertainty in the final state due to uncertainties in the ICs. In the next section, we quantify the uncertainty in the final state of the system calculating the fractal dimension and uncertainty exponent of the basins of attraction using different methods.

5. Fractal dimension and uncertainty exponent

We have further investigated the basins to better characterize their properties as fractal basins. Focusing on the region of the basins with the intermingled attractors, we have determined the fractal dimension D [20] and the uncertainty exponent α [22]. The fractal dimension was calculated directly, using the *box counting method* [20], and indirectly, from its relation to α.

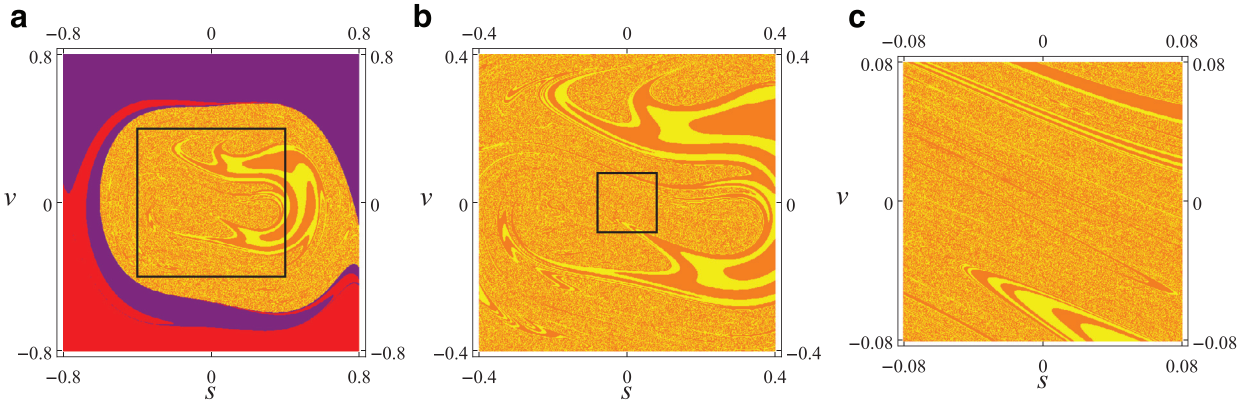

Fig. 5. (a) Basins of attraction for varying initial conditions s and v. Results for the parameters $V_{AC} = 0.8$ V, $V_{DC} = 17.9$ V, $\zeta = 0.6$, and $\beta = 0.01$. In (b) it is shown a magnification of the area delimited by the black square in (a), while (c) corresponds to a magnification of the black square in (b), both showing intermingled attractors of periods one and three. Color code is the same as that presented in the caption of Fig. 3.

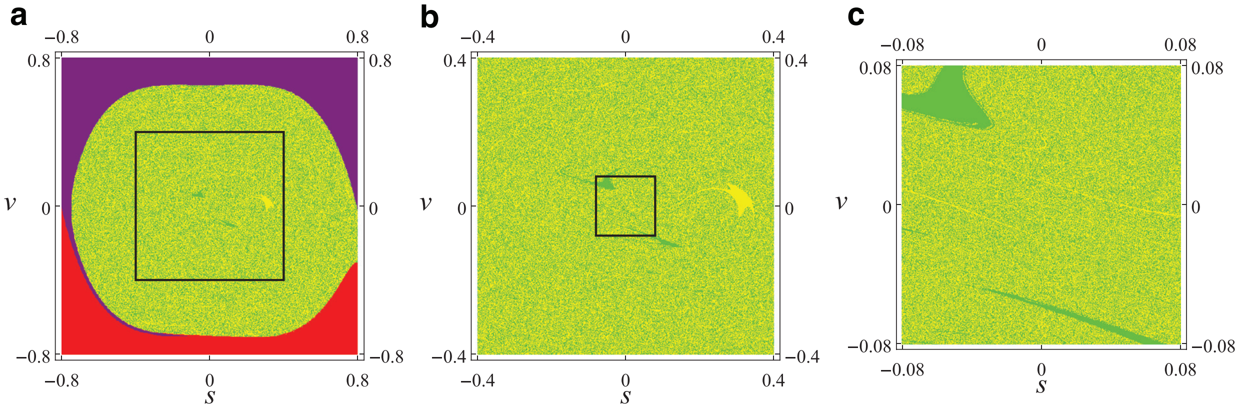

Fig. 6. (a) Basins of attraction for varying initial conditions s and v. Results for the parameters $V_{AC} = 0.3$ V, $V_{DC} = 17.5$ V, $\zeta = 0.3$, and $\beta = 0.01$. In (b) it is shown a magnification of the area delimited by the black square in (a), while (c) corresponds to a magnification of the black square in (b), both showing intermingled attractors of periods one and two. Color code is the same as that presented in the caption of Fig. 3.

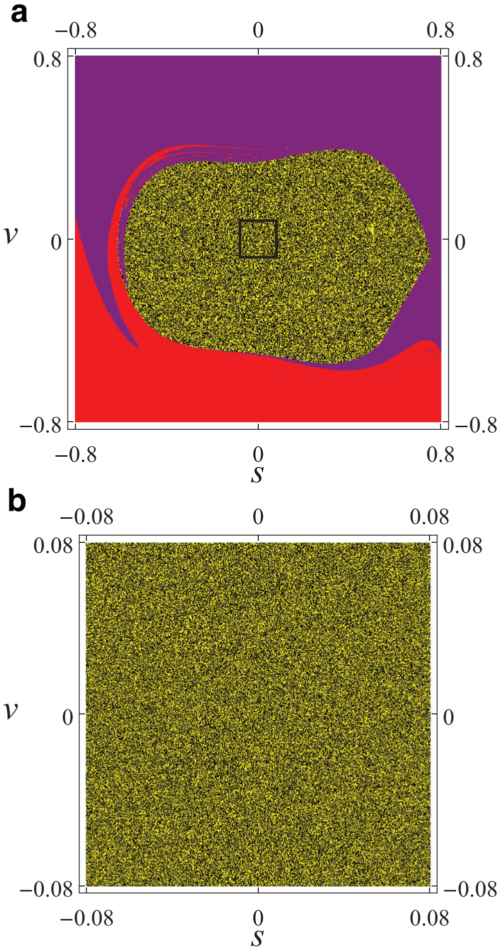

Fig. 7. (a) Basins of attraction for varying initial conditions s and v. Results for the parameters $V_{AC} = 1.0$ V, $V_{DC} = 18.5$ V, $\zeta = 0.4$, and $\beta = 0.01$. In (b) it is shown a magnification of the area delimited by the black square in (a) showing intermingled attractors of period one and chaos. Color code is the same as that presented in the caption of Fig. 3.

The box counting dimension (BCD) was calculated considering that the area of interest is formed by a regular grid of $M \times M$ points. We take 2D boxes (squares) with lateral size $\epsilon = n/M$, where n is a natural number that results in an integer value for $1/\epsilon$, so that the 2D boxes cover the area completely. We then count the number N of boxes required to cover either of the basins or the basin boundary, depending on the region for which we want to determine D. The BCD is defined by

$$D_{BC} = \lim_{\epsilon \to 0} \frac{\ln N(\epsilon)}{\ln\left(\frac{1}{\epsilon}\right)}, \tag{9}$$

and D_{BC} is obtained as the angular coefficient of the linear least squares fit (LLSF) of a first order polynomial to the pair of points $(\ln(1/\epsilon), \ln N(\epsilon))$ for the smallest possible values of ϵ. The dimension is obtained in the form $D_{BC} \pm \delta D_{BC}$, where the uncertainty is that from the least squares fit.

The uncertainty exponent was calculated using two different methods. One is the original *uncertainty method* proposed by McDonald et al. [22]. Following this method, within the region of interest we find a total of 10.000 randomly chosen ICs that lead to one of the attractors in the basin. Within a circle of small radius $\delta = \sqrt{ds^2 + dv^2}$, centered at each one of the ICs in the form (s_i, v_i), with $i = 1, \ldots, 10.000$, two other ICs are chosen randomly. If either one of these new ICs lead to a different attractor, then the corresponding original IC is counted as uncertain. After all 10.000 ICs are tested a fraction $f(\delta)$ results to be uncertain. These calculations are repeated 10 times for each δ, which varied from 10^{-1} down to 10^{-10}. Since α is defined by

$$\alpha = \lim_{\delta \to 0} \frac{\ln f(\delta)}{\ln \delta}, \tag{10}$$

the uncertainty exponent and its error are obtained from the LLSF of a first order polynomial to the pairs of points $(\ln \delta, \ln f(\delta))$, with the estimated uncertainty on $f(\delta)$ at each point taken into account.

We have also employed a new approach to calculate α. It is based on the recently proposed method for the calculation of basin entropy [23]. This entropy is calculated assuming that the basin is formed by a regular grid of $M \times M$ points. Each point can correspond to one of the N_A attractors in the basin. Similarly to what is done in the *box counting method*, the basin is covered with a regular grid of N 2D boxes with lateral size $\epsilon = n/M$, with n a natural number. The fraction of the points pertaining to the attractor j $(j = 1, \ldots, N_A)$ in the ith box, $p_{i,j}$, is then evaluated for each box. The basin entropy is then given by [23]

$$S_b = \frac{1}{N} \sum_{i=1}^{N} \sum_{j=1}^{N_A} p_{i,j} \ln\left(\frac{1}{p_{i,j}}\right). \tag{11}$$

S_b was originally conceived to quantify the complexity of basins of attraction. However, it was argued in [23] that for basins with a single boundary between attractors, as it is the case for the regions of the basins we want to characterize which have only two attractors, we can expect the following relation

$$\ln[S_b(\epsilon)] = \alpha_{BE} \ln(\epsilon) + \ln\left(\frac{n}{\tilde{n}} \ln 2\right). \tag{12}$$

In this expression, the ratio $\frac{n}{\tilde{n}}$ is proportional to the basin boundary and is expected to be a constant, while α_{BE} is the uncertainty exponent, which we distinguish with the subscript BE to indicate that it is calculated from the basin entropy.

The above relation was obtained by Daza et al. [23] from Eq. (11) as a special case (that of a single boundary) of a more general relation derived assuming that for boundaries between different basins of attraction the $p_{i,j}$ for the boxes covering the boundaries occur much more frequently with values around $p_{i,j} = 1/m$, with m the number of attractors within a box. Therefore, it is assumed that the case of an equiprobable distribuition of attractors within a box prevails in the distribution of the $p_{i,j}$. Specializing to the case of only two distinct basins of attraction and following Daza et al. [23], we consider that out of the N boxes covering the basin only N_2 boxes are covering the boundary between to attractors ($j = 1, 2$ in this case). Taking the approximation that they all have the same $p_{i,j} = 1/2$, we arrive at $S_b = (N_2/N) \ln 2$. Because N_2 scales as $n\epsilon^{-D}$ and N as $\tilde{n}\epsilon^{-d}$, where n and $\tilde{n}$ are constants of proportionality, D the dimension of the boundary and d that of the basin, Eq. (12) follows trivially as $\alpha = d - D$ [22].

As the result in Eq. (12) is based on an approximation that was not fully justified in [23], we have checked if it is a good approximation. Taking the basins for which we calculate the fractal dimension of the basin boundaries (see Section 5.1) we performed the statistics of the values of the $p_{i,j}$ $(j = 1, 2)$ within the boxes containing points pertaining to the two attractors. That means, boxes with $p_{i,j} = 0$ or $p_{i,j} = 1$ are excluded, living only boxes containing points pertaining to the boundary. We observed that the $p_{i,1}$ and $p_{i,2}$ follow Gaussian-like distributions that are highly concentrated around its mean values $\bar{p}_{i,1}$ and $\bar{p}_{i,2}$. In fact, because $p_{i,1} + p_{i,2} = 1$, the two distributions are not independent. Because the two basins do not occur at equal proportions, the mean is not equal to 1/2, but assume values that are close to it. Nonetheless, as long as the $p_{i,j}$ are concentrated around the given averages, we can extend the reasoning of Daza et al. [23] and conclude that $S_b = (N_2/N)(\bar{p}_{i,1} \ln(1/\bar{p}_{i,1}) + \bar{p}_{i,2} \ln(1/\bar{p}_{i,2})) = (N_2/N) \times constant$.

This more realistic approximation to S_b still results in a linear relation between $\ln(S_b)$ and $\ln(\epsilon)$ having α_{BE} as its angular coefficient. It is interesting to note, however, that we can always write the basin entropy in the form $S_b = (N_2/N) \times constant$, which assures the expected linear relation, independently of the statistical distribution of the $p_{i,j}$. This is shown in Appendix A.

The expected linear relation between $\ln(S_b)$ and $\ln(\epsilon)$ in Eq. (12) can be used to calculate α_{BE} from S_b evaluated for various ϵ's using a LLSF. As in the case of D_{BC}, the error estimate for α_{BE} comes from the uncertainty in the least squares fit.

This last method, which we refer as the *basin entropy method*, is a new approach to estimate α. So far, it has been used only to estimate α for a non-fractal basin of attraction, in which case $\alpha = 1$ [23]. Here, we compare the results obtained using the *box counting method* and the *uncertainty method* with the *basin entropy method*. We can thus check the reliability of the new method. The comparison between the three methods is possible because of the expected relation between α and the dimension of the basin boundary, $D = d - \alpha$, where d is the dimension of the space in which the fractal structure is embedded [22]. In our case $d = 2$.

5.1. Results

The calculations of D and α have been performed for the three basins of attraction presented in Figs. 5–7. More specifically, we have restricted the analysis to the region with the mixed attractors, and ignored the region with pull-in, because the ICs of real systems are almost certainly restricted to this region. The BCD and α_{BE} were, therefore, calculated for the regions presented in Figs. 5(b) and (c), 6(b) and (c), and 7(b). Both D_{BC} and α_{BE} were calculated using grids of resolution 800 × 800. We also performed calculations for some grids of resolution 1600 × 1600, which take much more computational time to be evaluated, that we compare with the results for the grids with lower resolution. The exponent α was calculated using the *uncertainty method* restricting the region where the random pairs of ICs were generated to that encompassed by the regions in Figs. 5(b) and 6(b), and to the square $-0.3 < s, v < 0.3$ for the basin depicted in Fig. 7(a). We are assuming that these areas are representative of the whole region where the periodic and chaotic basins are intermingled. The calculations over the smaller regions, that correspond to a larger magnification, have been done to check the scale invariance expected for fractal basins. In the next sub-sections we present the results for each basin separately.

5.1.1. Case $V_{AC} = 0.8$ V, $V_{DC} = 17.9$ V, and $\zeta = 0.6$

The BCD for the period-1 and period-3 basins in Fig. 5(b) are, respectively, $D_{BC} = 1.88 \pm 0.03$ and $D_{BC} = 1.94 \pm 0.01$. A similar result is obtained for the magnified region in Fig. 5(c), in which case we obtain $D_{BC} = 1.88 \pm 0.03$ (period-1) and $D_{BC} = 1.96 \pm 0.01$ (period-3). The BCD for the basin boundary was $D_{BC} = 1.80 \pm 0.04$ and $D_{BC} = 1.84 \pm 0.04$, for the regions in Figs. 5(b) and (c), respectively. The fact that $D_{BC} < 2$ for the period-1 and period-3 basins and significantly larger than 1 for the basin boundary and the consistency between the results for the larger area and its magnified portion are results expected for a fractal basin.

Using the *uncertainty method* we obtained $\alpha = 0.078 \pm 0.001$ which corresponds to a basin boundary dimension of $D_{UM} = 1.921 \pm 0.001$. This value for α is small, and can be interpreted as reflecting a significant uncertainty regarding which could be the periodic state assumed by the system for uncertain initial conditions. We note that D_{UM} is significantly larger than the dimension of the basin boundary obtained using the *box counting method*. The apparent discrepancy can be attributed to the inherent imprecision of the last method to determine the fractal dimension of curves and boundaries. The BCD calculated numerically for one or two dimensional systems frequently results in dimensions that are wrong by an actual error that is more than twice the error estimated from the least squares fit [24]. The actual discrepancy tends to be particularly large in the calculation of the dimension for curves in a 2D space, as it is the case of the basin boundary [24]. The estimated D_{BC} can be easily reconciled with the more precise result obtained using the *uncertainty method* taking into account the extra uncertainty.

In the course of the analysis to obtain α_{BE} from Eq. (12) we have found that some care must be taken for the extraction of correct results. Eq. (12) suggests a linear relation between $\ln[S_b(\epsilon)]$ and $\ln(\epsilon)$, however, quite generally, we have found that the data does not fit well to a straight line when the results for small ϵ are included. This is illustrated by the results presented in Fig. 8(a),

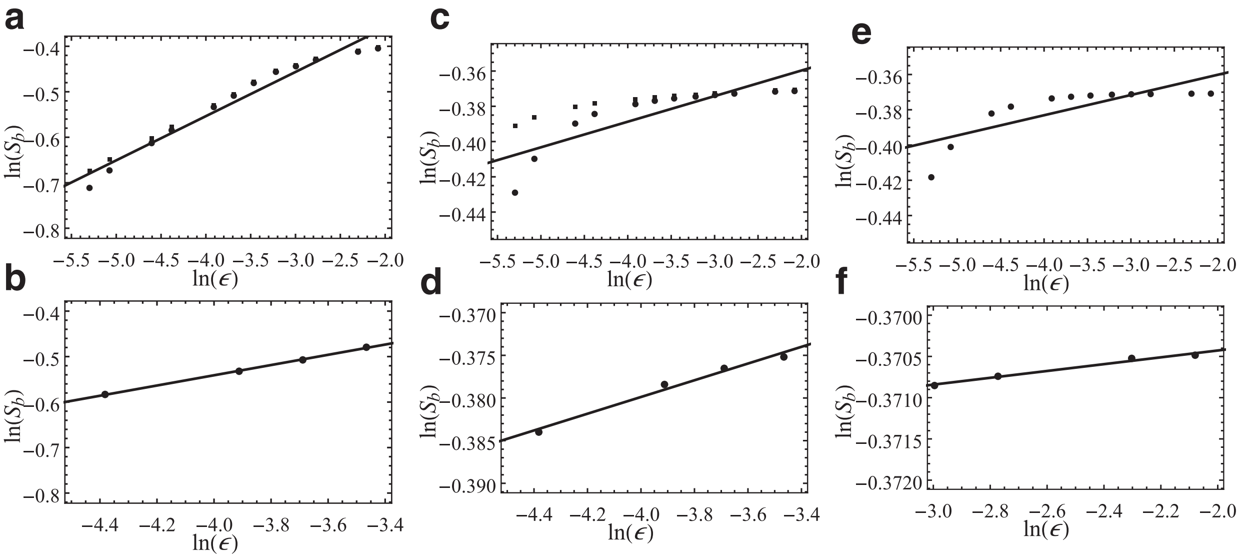

Fig. 8. In (a), (c), and (e) the circles (squares) correspond to points obtained for different box sizes ϵ corresponding a lateral size ranging from $n = 4(8)$ up to $n = 100(200)$ pixels for a grid of $800 \times 800 (1600 \times 1600)$ pixels. The line is the result of the least squares fit for the circles. In the lower panels we have the same as in (a), (c), and (e) but for ϵ corresponding to boxes with lateral size ranging from $n = 10$ up to $n = 25$ pixels ((b) and (d)) and $n = 40$ up to $n = 100$ (f). From the left to the right panels the results are for the basins analyzed in Sections 5.1.1, 5.1.2, and 5.1.3.

(c), and (e). The reason for such nonlinear behavior and how it is circumvented is addressed at the Section 6. What we concluded is that when intermediate values of ϵ are used, we obtain either good or very good fits, depending on the basin being analyzed. In all cases, the magnitude of the obtained values for α_{BE} represent a good estimate for the uncertainty exponent, as we are going to see next.

To determine α_{BE} for the basin analyzed in this subsection, we have ignored the smallest ϵ's, and included in the fit the points resulting in a sufficiently small fitting error. In this case we considered the points obtained for boxes with size 10×10 up to 25×25 pixels, obtaining the fitted line shown in Fig. 8(b). The resulting uncertainty exponent is $\alpha_{BE} = 0.112 \pm 0.002$ for the basin in 5(b). In this case, the line fitting is very good and the result is in fair agreement with $\alpha = 0.078 \pm 0.001$ obtained using the *uncertainty method*. It is worth to note that, for this basin, if we include larger ϵ in the fitting, a smaller α_{BE} is obtained, leading to a slightly better agreement with α, but the fitting error increases significantly, indicating that the result may be less reliable. We have also applied the *basin entropy method* to the magnified region shown in 5(c). For this basin we observe a larger influence of a nonlinear dependence on $\ln \epsilon$, and the line fitting is not so accurate. However, performing the fitting within the same range of ϵ we obtain $\alpha_{BE} = 0.048 \pm 0.004$. This result still reflects the significant uncertainty expected for this region of the basin.

5.1.2. Case $V_{AC} = 0.3$ V, $V_{DC} = 17.5$ V, and $\zeta = 0.3$

The BCD for the period-1 and period-2 basins in Fig. 6(b) are, respectively, $D_{BC} = 1.97 \pm 0.01$ and $D_{BC} = 1.95 \pm 0.02$. For the magnified region in Fig. 6(c), we obtain $D_{BC} = 1.96 \pm 0.01$ (period-1) and $D_{BC} = 1.95 \pm 0.02$ (period-2). For the basin boundary we obtain $D_{BC} = 1.93 \pm 0.03$ and $D_{BC} = 1.92 \pm 0.03$, for the regions in Figs. 6(b) and (c), respectively. Again, the value of the dimensions and the consistency between the results for the larger area and its magnified portion indicates that the region with intermingled basins has a fractal structure. However, in this case, the dimension of the basins and the basin boundary are significantly closer to 2, a result that reflects the qualitative observation that the basin has two attractors that are strongly intermingled.

Using the *uncertainty method* we obtained $\alpha = 0.0085 \pm 0.0001$ which corresponds to a basin boundary dimension of $D_{UM} = 1.9915 \pm 0.0001$. This value of α is significantly smaller than that of the previous basin. It reflects the even larger uncertainty regarding which could be the periodic state assumed by the system for uncertain initial conditions.

While for the previous basin of attraction we obtained a very good line fitting to the data for Fig. 5(b), for both the basin in Fig. 6(b) and the magnified area in (c), there is a stronger nonlinear contribution. From the fit to the points obtained for boxes with size of 10×10 up to 25×25 pixels shown in Fig. 8(d), we obtained $\alpha_{BE} = 0.010 \pm 0.001$ for the basin in 5(b). In this case, the line fitting is good, as can be seen in Fig. 8(d), and the result is in fair agreement with α obtained using the *uncertainty method*. For the magnified region we obtain $\alpha_{BE} = 0.015 \pm 0.001$, which is close to the exponent obtained for the larger area, and a reasonable result that reflects the significant uncertainty of the basin.

5.1.3. Case $V_{AC} = 1.0$ V, $V_{DC} = 18.5$ V, and $\zeta = 0.4$

The BCD for the period-1 and chaotic basins in Fig. 7(b) are, respectively, $D_{BC} = 1.97 \pm 0.01$ and $D_{BC} = 1.95 \pm 0.02$. For the basin boundary we obtain $D_{BC} = 1.93 \pm 0.03$. While this basin of attraction seems to have a stronger mixing of the two attractors, the BCDs are the same as those obtained for the previous basin. Therefore, we can see that while the *box counting method* has the advantage of providing the fractal dimension of the basins of each attractor, this result shows the limitations of the method to characterize the fractal properties of a basin of attraction, and the need to complement the information using the other methods we are considering.

Table 1
Fractal dimension of the basin boundaries obtained using *box counting*, *uncertainty method*, and *basin entropy*, for the basins depicted in the figures listed below.

Basin	Box counting	Uncertainty	Basin entropy
Fig. 5(b)	1.80 ± 0.04	1.921 ± 0.001	1.888 ± 0.002
Fig. 6(b)	1.93 ± 0.03	1.9915 ± 0.0001	1.990 ± 0.001
Fig. 7(b)	1.93 ± 0.03	1.9997 ± 0.0001	1.99959 ± 0.00004

Using the *uncertainty method* we obtained $\alpha = 0.0003 \pm 0.0001$ which corresponds to a basin boundary dimension of $D_{UM} = 1.9997 \pm 0.0001$. This α is very small, characteristic of a basin with extremely intermingled attractors, and reflects the extreme uncertainty regarding the final state assumed by the system for uncertain initial conditions.

As for the basin in Section 5.1.2, there is a comparatively strong nonlinear dependence on ϵ observed in the calculation using the *basin entropy method*. From the fit to the points obtained for boxes with the same size considered previously of 10×10 up to 25×25 pixels, we obtained $\alpha_{BE} = 0.0070 \pm 0.0013$. Differing from the previous results, which where in reasonable numerical agreement with α obtained using the *uncertainty method*, in this case the *basin entropy method* misses the actual value by an order of magnitude. The result obtained using this range of box dimensions also has a significant uncertainty of about 20%. The results presented in Fig. 8(e) indicate that for larger ϵ (less negative $\ln(\epsilon)$) the points tend to be more aligned. In fact, using the range of points corresponding to larger boxes of size 40×40 up to 100×100 pixels results in a best fit, shown in Fig. 8(f). In this case we obtain $\alpha_{BE} = 0.00041 \pm 0.00004$. Therefore, the error has been reduced to 10% and the result agrees very well with α obtained using the *uncertainty method*.

For the sake of clarity, we present in Table 1, the fractal dimension obtained using the three different methods for the basins analyzed in the Section 5.1.

6. Discussion and conclusions

MEMS/NEMS resonators have many potential applications of their nonlinear behavior [3,4,8,12]. However, these applications and possibly new applications, require an adequate understanding of the nonlinear behavior of such systems. Compared to the results presented in [10] in this work we have presented new results, in the form of phase diagrams, that help to better understand what nonlinear behavior to expect for doubly clamped suspended beam MEMS/NEMS resonators. We have determined that the most rich dynamics starts to show up when the effective potential comes closer to the separatrix between one and double-well regions. The phase diagrams have revealed the existence of an intricate dependence of the dynamics on the relevant control parameters V_{AC}, V_{DC}, and ζ, showing the complex regions with periodic behaviour, chaos and pull-in, which have not been investigated in [10]. The observed dependence is even more complex for lower dissipation, with the different attractors getting more intermingled. This makes it much more difficult to predict the final state of the system. Also, the lower dissipation favors the appearance of more complex dynamics farther away from the separatrix, in the region with smaller values of V_{DC}.

Also, a better definition of the regions with chaos, compared with the results presented in [10], have been obtained. This information is relevant, for instance, for applications of this system as a source of chaotic signals. With the analysis in the present work we have been able to concluded that chaos is more easily obtained for lower excitation frequencies and higher dissipation.

We have performed a detailed investigation of the basins of attraction of this system that was missing in previous works in the literature. We found that in the regions with evidences of multistability basins of attraction with fractal structures occur quite frequently. The fractality was confirmed through the calculation of the chaotic saddle and quantified through the calculation of the fractal dimensions of the basins and its boundary, and the uncertainty exponent. The high fractal dimensions found for the basins investigated in Sections 5.1.2 and 5.1.3, close to $D = 2$, and the very low α indicate that we have found extremely intermingled basins. This results, in practical implementations of the system, in an absolute uncertainty regarding the final state of the system if care is not taken to be away from the regions were such basins exist.

In the analysis of the basins we have used a new method to determine the uncertainty exponent, namely, the *basin entropy method*. This method was originally conceived to quantify the complexity of the basins of attraction. Larger entropies S_b are expected to indicate more complex basins, with consequent larger uncertainties regarding the final state of the system. This expectation is confirmed by the results presented in Fig. 8 (a), (c), and (e). In such figures S_b obtained for a given ϵ is much large for the two basins with visibly more intermingled basins (note that a less negative $\ln(S_b)$ corresponds to a larger S_b). The entropies in Fig. 8(e) are also slightly larger than that depicted in Fig. 8(c) as it would be expected based on the results of Sections 5.1.2 and 5.1.3.

An important fact, regarding the use of S_b to estimate α, is the observation of a nonlinear dependence between $\ln[S_b(\epsilon)]$ and $\ln \epsilon$, instead of the linear dependence expected according to Eq. (12). We have found that the origin of this nonlinearity is the finite resolution of the grid. The expected linear relation in Eq. (12), assumes, implicitly, an infinite resolution in the calculation of S_b. That means, the areas of each basin contained within a 2D box of lateral side ϵ are known with infinite precision. However, the actual calculations are based on areas estimated with a coarseness. In order to address the effect of the finite resolution we have generated the basins analyzed in Sections 5.1.1 and 5.1.2 with a finer grid with resolution 1600 × 1600 pixels. What we observed is that for the smaller range of ϵ's the entropy estimated with lower resolution is significantly smaller than that obtained with a finer grid resolution. As ϵ increases, the discrepancy between the calculations with different resolutions becomes very small. This effect is illustrated by comparing the points obtained with the two resolutions in Figs. 8(a) and (c). The points for the finer grid resolution come much closer to expected linear distribution. Therefore, in order to get a correct estimate of α_{BE} using grids with lower resolution, what is desirable since the computational times is smaller, small ϵ's must be disregarded. As a practical rule, we suggest that the lateral size of the 2D boxes must be at least of 10 pixels for basins covered with a grid of 800 × 800 pixels, as we have considered in our calculations of α_{BE}.

Using intermediate values of ϵ we have obtained very good estimates of α with the *basin entropy method* using basins calculated with a grid resolution that demands a reasonable computational time. We conclude, therefore, that it is an adequate alternative method to calculate α. The new approach deserves a more systematic study in order to further investigate its reliability and precision, and to address its computational efficiency compared to other methods, which is beyond the scope of the present work.

Further theoretical and experimental investigation of the system we investigated is required for a complete understanding of its dynamics. The effect of longitudinal prestress on the phase diagram and basins would be interesting to be analyzed, since small stresses are usually present in micro and nanofabricated devices. However, as the approximate dynamical equation describing the system retains the same form, similar results should be expected for small prestress. The influence of noise, which can be significant for the smaller NEMS resonators [19], has not been studied so far. Also, recent experimental [25] and theoretical [26,27] results indicate that nonlinear damping can be large in such systems. As the nonlinear damping generally increases with the amplitude of vibration, it could play a significant role in the total dissipation in the strong nonlinear regime that we have investigated in this work, where the amplitudes of vibration are high compared to the beam thickness. The recent theoretical prediction that two-frequency excitation can result in robust chaos in this system [15] should also motivate further theoretical investigations of MEMS/NEMS resonators.

Declaration of interests

The authors declare that they have no known competing financial interests or personal relationships that could have appeared to influence the work reported in this paper.

Acknowledgments

ACM acknowledges the financial support from CNPQ-Brasil through a postdoctoral fellowship grant (grant 150112/2018-1). AG is thankful to WG Dantas (VCE-UFF) for useful discussions and contributions. RLV was supported by CNPq-Brasil. ILC was supported by FAPESP (grant 2018/03211-6).

Appendix A. Proof of a general linear relation between $\ln S_b$ and $\ln \epsilon$, with angular coefficient α_{BE}

In this proof we consider that the region containing the two basins of attraction is covered with a regular grid of N square boxes of side ϵ.

We start the proof by noting that since we have only two attractors (1 and 2) and the $p_{i,j}$ in Eq. (11) must satisfy $p_{i,1} + p_{i,2} = 1$, the basin entropy can be written as

$$\begin{aligned} S_b &= -\frac{1}{N}\sum_{i=1}^{N}(p_{i,1}\ln p_{i,1} + p_{i,2}\ln p_{i,2}) \\ &= -\frac{1}{N}\sum_{i=1}^{N}\{p_i[\ln p_i - \ln(1-p_i)] + \ln(1-p_i)\} = -\frac{1}{N}\sum_{i=1}^{N} S_i, \end{aligned} \tag{A.1}$$

where, for simplicity, we have taken $p_i = p_{i,1}$.

Now, we take into account that in any real computation the basin is discretized into pixels. We consider pixels with equal size, and each square box containing N_p^2 pixels, where N_p is the number of pixels comprised in the length ϵ. Consequently, for any given box the p_i can only assume one out of a set of discrete values $p_i = 0, 1/N_p^2, 2/N_p^2, \ldots, 1 - 1/N_p^2, 1$. The boxes with $p_i = 0$ or 1 do not contribute to S_b, because $S_i = 0$ in such cases. What is left is the contribution of the boxes at the boundary, those containing pixels of both attractors. Therefore, the possible values of the p_i for the remaining N_2 boxes are

$$p_m = \frac{m}{N_p^2}, \quad m = 1, \ldots, N_p^2 - 1. \tag{A.2}$$

Noting that it is always true that a certain fraction q_m of the N_2 boxes covering the boundary has a basin probability p_m, the basin entropy can be written as

$$S_b = -\frac{1}{N}\sum_{m=1}^{N_p^2-1} q_m N_2 S_m = -\frac{N_2}{N}\sum_{m=1}^{N_p^2-1} q_m S_m = -\frac{N_2}{N} \times C. \tag{A.3}$$

The constant C appearing in the last expression depends upon the particular distribution q_m. In the case of the fractal basins we have investigated, the q_m concentrate around a mean value with a Gaussian-like distribution. It is interesting to note, however, that for the more regular basins of attraction for the damped Duffing oscillator investigated by Daza et al. [23] (see their Fig. 3 (a)-(c)) the p_m are distributed more evenly, independently of the box resolution N_p.

To complete the proof we can now simply follow the reasoning used by Daza et al. [23] and consider that N_2 scales as $n\epsilon^{-D}$ and N as $\tilde{n}\epsilon^{-d}$, where D and d are, respectively, the dimensions of the basin boundary and that of the basin. Therefore,

$$S_b = \frac{n}{\tilde{n}}\epsilon^{d-D} \times constant = \frac{n}{\tilde{n}}\epsilon^{\alpha_{BE}} \times C\,, \tag{A.4}$$

and a generalized linear relation follows

$$\ln[S_b(\epsilon)] = \alpha_{BE} \times \ln(\epsilon) + \ln\left(\frac{n}{\tilde{n}}C\right). \tag{A.5}$$

We have thus concluded that for basins containing only two attractors we can always expect a linear relation between $\ln[S_b(\epsilon)]$ and $\ln(\epsilon)$, in which the angular coefficient can be interpreted as the uncertainty exponent.

References

[1] Huang XMH, Feng XL, Zorman CA, Mehregany M, Roukes ML. VHF, UHF and microwave frequency nanomechanical resonators. New J Phys 2005;7:247. doi:10.1088/1367-2630/7/1/247.

[2] Uranga A, Verd J, Barniol N. CMOS-MEMS resonators: from devices to applications. Microelectron Eng 2015;132:58–73. doi:10.1016/j.mee.2014.08.015.

[3] Almog R, Zaitsev S, Shtempluck O, Buks E. Signal amplification in a nanomechanical duffing resonator via stochastic resonance. Appl Phys Lett 2007;90:013508. doi:10.1063/1.2430689.

[4] Antonio D, Zanette DH, López D. Frequency stabilization in nonlinear micromechanical oscillators. Nat Commun 2012;3:806. doi:10.1038/ncomms1813.

[5] Rhoads J, Shaw SW, Turner KL. Nonlinear dynamics and its applications in micro- and nanoresonators. In: Proceedings of 2008 ASME Dynamic Systems and Control Conference,October 20–22; 2008. Ann Arbor, Michigan, USA.

[6] De S K, Aluru NR. Complex oscillations and chaos in electrostatic microelectromechanical systems under superharmonic excitations. Phys Rev Lett 2005;94:204101. doi:10.1103/PhysRevLett.94.204101.

[7] Amorim TD, Dantas WG, Gusso A. Analysis of the chaotic regime of MEMS/NEMS fixed–fixed beam resonators using an improved 1DOF model. Nonlinear Dyn 2015;79:967–81. doi:10.1007/s11071-014-1715-4.

[8] Barceló J, Rosselló JL, Bota S, Segura J, Verd J. Electrostatically actuated microbeam resonators as chaotic signal generators: a practical perspective. Commun Nonlinear Sci Numer Simulat 2016;30:316–27. doi:10.1016/j.cnsns.2015.06.032.

[9] Alemansour H, Miandoab EM, Pishkenari HN. Effect of size on the chaotic behavior of nano resonators. Commun Nonlinear Sci Numer Simulat 2017;44:495–505. doi:10.1016/j.cnsns.2016.09.010.

[10] Dantas WG, Gusso A. Analysis of the chaotic dynamics of MEMS/NEMS doubly clamped beam resonators with two-sided electrodes. Int J Bifurc Chaos 2018;28:1850122. doi:10.1142/S0218127418501225.

[11] Karabalin RB, Cross MC, Roukes ML. Nonlinear dynamics and chaos in two coupled nanomechanical resonators. Phys Rev B 2009;79:165309. doi:10.1103/PhysRevB.79.165309.

[12] Wang YC, Adams SG, Thorp JS, MacDonald NC, Hartwell P, Bertsch F. Chaos in MEMS, parameter estimation and its potential application. IEEE Trans Circuits Syst I 1998;45:1013–20. doi:10.1109/81.728856.

[13] Haghighi HS, Markazi AHD. Chaos prediction and control in MEMS resonators. Commun Nonlinear Sci Numer Simulat 2010;15:3091–9. doi:10.1016/j.cnsns.2009.10.002.

[14] Siewe MS, Hegazy UH. Homoclinic bifurcation and chaos control in MEMS resonators. Appl Math Model 2011;35:5533–52. doi:10.1016/j.apm.2011.05.021.

[15] Gusso A, Dantas WG, Ujevic S. Prediction of robust chaos in micro and nanoresonators under two-frequency excitation. Chaos 2019;29:033112. doi:10.1063/1.5058750.

[16] Younis MI. MEMS linear and nonlinear statics and dynamics. New York: Springer; 2011.

[17] Fu Y, Zhang J, Jiang Y. Influences of the surface energies on the nonlinear static and dynamic behaviors of nanobeams. Phys. E 2010;42:2268–73. doi:10.1016/j.physe.2010.05.001.

[18] Arecchi FT, Badii R, Politi A. Generalized multistability and noise-induced jumps in a nonlinear dynamical system. Phys Rev A 1985;32:402–8.

[19] Cleland AN. Foundations of nanomechanics. Berlin: Springer; 2002.

[20] Alligood KT, Sauer TD, Yorke JA. Chaos: an introduction to dynamical systems. New York: Springer; 1997.

[21] Aguirre J, Viana RL, Sanjuán MAF. Fractal structures in nonlinear dynamics. Rev Mod Phys 2009;81:333–86. doi:10.1103/RevModPhys.81.333.

[22] McDonald SW, Grebogi C, Ott E, Yorke JA. Fractal basin boundaries. Physica D 1985;17:125–53. doi:10.1016/0167-2789(85)90001-6.

[23] Daza A, Wagemakers A, Georgeot B, Guéry-Odelin D, Sanjuán MAF. Basin entropy: a new tool to analyze uncertainty in dynamical systems. Sci Rep 2016;6:31416. doi:10.1038/srep31416. (2016)

[24] Górskia AZ, Drozdza S, Mokrzyckac A, Pawlik J. Accuracy analysis of the box-counting algorithm. Acta Phys Pol A 2012;121:28–30. doi:10.12693/APhysPolA.121.B-28.

[25] Zaitsev S, Shtempluck O, Buks E, Gottlieb O. Nonlinear damping in a micromechanical oscillator. Nonlinear Dyn 2012;67:859–83. doi:10.1007/s11071-011-0031-5.

[26] Gusso A. Nonlinear damping in doubly clamped beam resonators due to the attachment loss induced by the geometric nonlinearity. J Sound Vib 2016;372:255–65. doi:10.1016/j.jsv.2016.02.044.

[27] Gusso A, Pimentel JD. Nonlinear damping in MEMS/NEMS beam resonators resulting from clamping loss. In: Proceedings of the sixth international conference on nonlinear science and complexity; 2016. São José dos Campos, Brazil, doi: 10.20906/CPS/NSC2016-0045.